Adaptive Multi-Output Model-Based Design of Experiments for Accelerated Lithium-Ion Battery Parameter Estimation

Palash Gaikwad[1], Daniel Brandell[2], Masood Tamadondar[1]

[1] Volvo Group Trucks Technology (GTT), 40508 Gothenburg, Sweden
[2] Department of Chemistry - Ångström Laboratory Uppsala University, 75121 Uppsala Sweden
Email:palash.gaikwad@volvo.com

Executive Summary

This work presents a novel framework for model-based design of experiments (MBDoE) for lithium-ion batteries, incorporating global and regional sensitivity metrics, adaptive experimental design, and thermal dynamics. Built on the PyBaMM simulation platform, the approach leverages Sobol indices, Kolmogorov-Smirnov-based Regional Sensitivity Analysis (RSA), and polynomial surrogate modeling to inform and optimize parameter identifiability. A time-segmented Fisher Information Matrix (FIM) scoring system tracks the temporal evolution of parameter observability, enabling targeted experimental refinement. The results demonstrate enhanced observability, adaptive design efficiency, and insights into thermal-electrochemical coupling.

Keywords: Batteries, Battery Management systems; Modelling and Simulation; Sobol; RSA; Battery Parameter Estimation

1 Introduction

Lithium-ion batteries are central to the transition toward sustainable energy systems, powering everything from portable electronics to electric vehicles and grid storage. Accurate physics-based modeling of these systems is critical for design, control, and health estimation [1]. However, the reliability of such models hinges on the identifiability of underlying parameters, which in turn depends heavily on the design of experiments (DoE) used to generate calibration data.

Model-Based Design of Experiments (MBDoE) offers a principled way to design informative tests by maximizing the information content relative to model parameters [2]. Traditional MBDoE techniques for lithium-ion batteries often rely on global Fisher Information Matrix (FIM) optimization, but typically neglect temporal dynamics, thermal coupling, and complex interaction effects. This work presents a comprehensive MBDoE framework that addresses these limitations by integrating:

- Global sensitivity analysis using Sobol indices
- Regional sensitivity analysis via Kolmogorov–Smirnov statistics
- Adaptive experiment refinement with lumped thermal model intergrated with Doyle-Fuller-Newman (DFN) models.
- Surrogate-assisted optimization for fast evaluations
- Time-segmented FIM scoring to localize parameter observability

Based on the PyBaMM simulation environment, this framework enables both offline and adaptive experimental design strategies. The inclusion of thermal modeling and multiple observables, such as voltage, dV/dt, and temperature, enhances the utility and realism of the method. The result is a robust experimental design strategy capable of guiding physical experiments toward improved parameter identifiability and reduced uncertainty.

2 Literature Review

Global sensitivity analysis (GSA) has emerged as a key tool for determining which inputs most significantly influence high-fidelity lithium-ion battery models such as Single Particle Model with electrolyte (SPMe) and the DFN framework. By quantifying how the uncertainty in each parameter—and their interactions—affects the model outputs under varying load conditions, GSA enables the fixation of low-impact parameters and focuses calibration on the few that dominate variance [3].

Furthermore, time-resolved GSA implies that parameter importance can shift over a discharge cycle,so experiments are designed in such a a way that to enhance parameter identifability [3]. Regional Sensitivity Analysis (RSA) complements GSA by dividing parameter ranges into low, mid, and high quantiles and uses Empirical Cumulative Distribution Function (ECDF) comparisons to uncover regime-specific sensitivities, refining the boundaries for parameters that matter signficantly only under certain conditions [4].

Model-based Design of Experiments (MBDoE) then leverages these insights to identify current and temperature profiles that maximize information gain. By optimizing the D-optimality criterion—i.e., the determinant of the Fisher Information Matrix—protocols can be tailored to render the most informative dynamics, outperforming standard constant-current or pulse tests for parameter identifiability [5,6].

Recent advances integrate GSA directly into MBDoE: sensitivity-weighted objectives ensure that influential parameters drive the design process, yielding robust protocols even in high-dimensional, nonlinear settings. Studies have demonstrated that GSA-informed MBDoE schemes achieve faster convergence and lower estimation error compared to designs based solely on local sensitivities [7,8].

3 Gaps in Literature and Novel Contribution

Despite progress, several gaps remain:

• Few studies implement time-resolved GSA in the experiment design.

• Multi-objective MBDoE accounting for parameter uncertainty is rare.

• Integration of RSA with MBDoE has not been reported in battery modeling.

• Adaptive MBDoE strategies remain underexplored in the battery context.

Our proposed framework addresses these gaps by introducing an adaptive RSA-informed MBDoE approach. RSA identifies sensitive parameter regions via ECDF and statistical filtering. These insights guide boundary refinement and influence the parameter selection. MBDoE is then used to design optimal input profiles, which iteratively update the sensitivity landscape. To our knowledge, this is the first work to integrate RSA, GSA, and adaptive MBDoE in lithium-ion battery modeling using PyBaMM.

4 Methodology

The complete flowchart is shown in Figure 1. Detailed explanations of each block is provided in the following subsections.
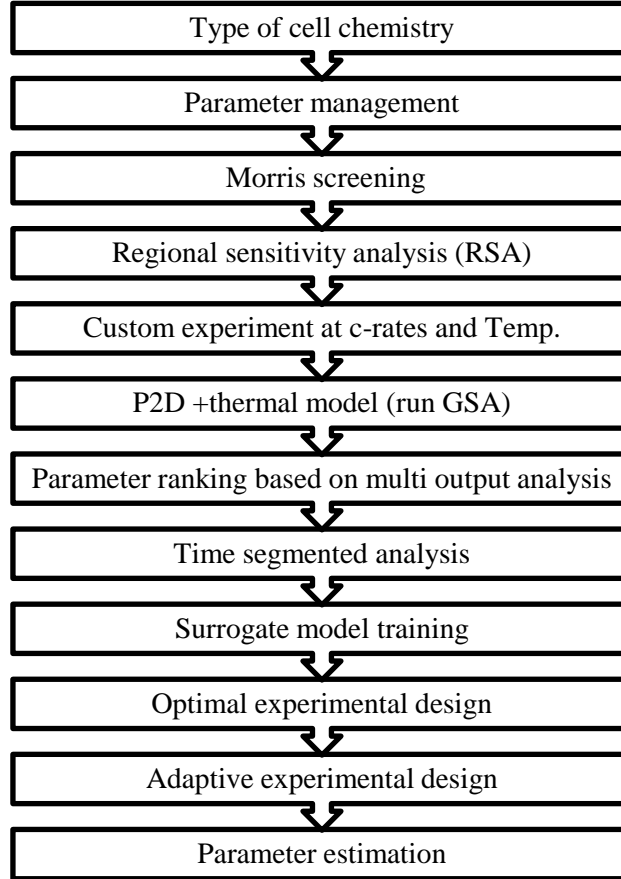

Figure 1: Multi-Output Adaptive MBDoE framework.

4.1 Parameter Space Extraction and Initialization

We begin by compiling the full DFN model augmented with a lumped thermal model as it remains the de facto standard for high-fidelity lithium-ion battery simulations [3]. From this parameter set, we extract 42 physio-chemical inputs—including exchange current densities, electrode porosities, electronic and ionic conductivities, solid-state and electrolyte diffusivities, and overall thermal properties, and apply ±50% bounds around each nominal value. We then nondimensionalize so that $\theta_i = 1$ corresponds exactly to its nominal value, yielding a dimensionless parameter vector $\theta \in \mathbb{R}^{42}$ with well-defined lower and upper limits for the following analyses.

4.2 Elementary-Effects (Morris) Screening

To rapidly screen out parameters with negligible first-order or interaction effects, we employ the Morris one-factor-at-a-time (OAT) method [5]. We generate r independent trajectories through the 42-dimensional parameter space, each perturbing one θ_i at a time by a fixed step Δ. The elementary effect for parameter i on a scalar output Y (e.g., peak voltage) in trajectory j is defined as $EE_i(j) = [Y(\theta + \Delta \cdot e_i) - Y(\theta)]/\Delta$. Computing $\mu_i = \text{mean}(|EE_i|)$ quantifies each parameter's main effect, while

σ_i = std(EE$_i$) captures non-linearity or interactions. Parameters exhibiting both low μ_i and σ_i are discarded, typically reducing the set to approximately 24 parameters where deeper analyses are necessary.

4.3 Global and Regional Sensitivity Analysis

For the retained parameters, we perform a variance-based Sobol analysis using a surrogate emulator to efficiently compute first-order (S$_{1,i}$) and total-effect (S$_{t,i}$) indices [8], identifying which θ_i that drive most of the output variance and which exhibit significant interactions.

$$S_{1,i} = \frac{Var_{\theta_i} E(Y|\theta_i)]}{Var(Y)} \qquad (1)$$

$$S_{T,i} = 1 - \frac{Var[Y(Y|\theta_i fixed)]}{Var(Y)} \qquad (2)$$

Concurrently, Regional Sensitivity Analysis (RSA) partitions each θ_i's samples into low, mid, and high quantiles and compares the output's empirical cumulative distribution function in each bin against the overall distribution using Kolmogorov–Smirnov statistics, thereby uncovering parameters that are influential only within specific subranges [4].

4.4 Time-Segmented Fisher Information Matrix Computation

To capture when each θ_i (each parameter) is most observable during a dynamic protocol, we divide the experiment timeline into H fixed windows. Within each window, we evaluate local sensitivities $J_{(k-j),i} = \partial y_k(t_j) / \partial \theta_i$ for each output k ∈ {voltage, state-of-charge (SOC), discharge capacity, temperature} at sampling times t$_j$, assemble the segment FIM as FIM^(h) = [J^(h)]^T W^(h) J^(h), and sum across windows to obtain the total FIM. The resulting time-resolved heatmaps reveal the specific phases during which each θ_i contributes maximum information [5].

4.5 Surrogate Model Training

Given the computational burden of repeated thermally dependent DFN runs in PyBaMM, we train two emulators—a LightGBM gradient-boosting machine for rapid objective evaluation [3] and a Gaussian process regressor for uncertainty quantification [6]—on approximately 1,000 Latin Hypercube-sampled (θ, u(t)) pairs. Both models achieve cross-validated R² > 0.95 and low mean absolute error, enabling fast approximations of model outputs for new parameter and protocol combinations.

4.6 MBDoE Objective and Loss Function

We define the multi-output MBDoE loss for a candidate protocol u(t) as

$$L_{(u;\theta)} = -\ln \det[FIM_{total}(u;\theta)] + \lambda_1 \sum_i (1 - S_{1,i})^2 + \lambda_2 \sum_i (S_{T,i} - S_{1,i})^2 \qquad (3)$$

Where:
- FIMtotal(u;θ) is the Fisher Information Matrix accumulated across all outputs (Voltage, Capacity, Temperature, SOC).
- S$_1$,i is the first-order Sobol sensitivity index for parameter i. S$_{T}$,i is the total Sobol sensitivity index for parameter i. Hyperparameters: λ_1, λ_2
- Objective :Main-effect coverage (make S$_1$ close to 1) ⇒ penalize (1–S$_1$)².Interaction minimization (keep S$_t$–S$_1$ small) ⇒ penalize strong interactions.

4.7 Adaptive MBDoE Loop

An adaptive loop iterates until credible parameter intervals converge. This is done through the follwing steps: (i) update Sobol and RSA metrics as θ posteriors evolve; (ii) optimize u(t) via augmented by surrogate-based gradient refinement; (iii) execute the optimized protocol and record responses $y_k(t)$; (iv) perform Bayesian updates using PyBOP to obtain new θ distributions [9]; and (v) retrain the surrogates with the new data. The loop terminates when the convergence criteria on FIM eigenvalues or posterior variances are satisfied i.e MBDoE loss change is $\Delta L < (10^{-2}$ to $10^{-3})$.

4.8 Bayesian Parameter Estimation

After the adaptive loop, all collected data are fused for final Bayesian inference. We draw samples from the posterior distribution p(θ | {u(k), y(k)}) using (Markov Chain Monte Carlo (MCMC), compute posterior means and credible intervals, and analyze ECDFs of estimation errors to fully quantify θ estimates and their uncertainties [8].

5. Result

5.1 Parameter Bounds and Selection (Morris screening process)

In order to reduce the burden of carrying out sensitivity analysis on all parameters of the Chen2020 [3] set used for the physics-based NMC ($LiNi_xMn_yCo_zO_2$) battery chemistry model, we performed Morris screening. All parameters were varied in the range 0.5-1.5 times there nominal value, and the standard deviation and mean elementary effects were analyzed. The top 24 parameters were selected and grouped into categories. The detail table is given in the Appendix.
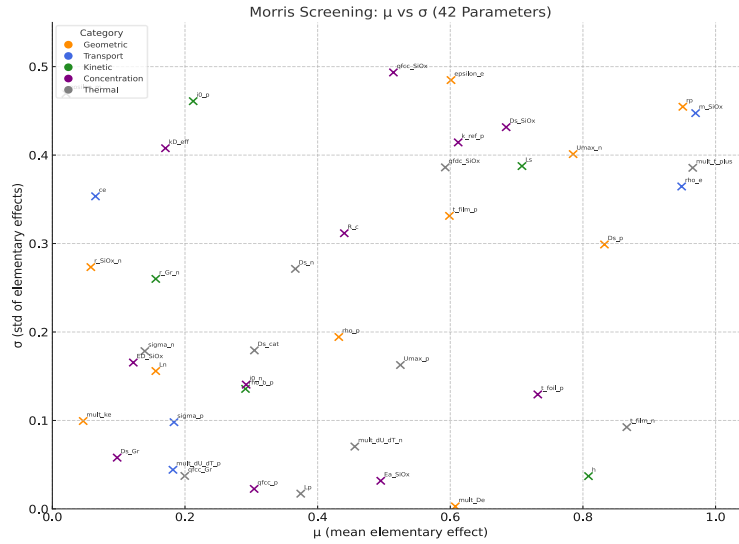

Figure 2: Morris Screening (μ vs σ)

In Figure 2, the plot of Morris mean effects (μ_i) versus standard deviations (σ_i) check for the most influential parameters, demonstrating that perturbations in these inputs produce large, repeatable changes in the model outputs. The moderate σ_i values imply that their effects are predominantly first-order, with limited higher-order interactions, thus simplifying the downstream sensitivity analyses. Parameters such as the Solid Electrolyte Interphase (SEI) resistance cluster near the origin (μ<0.10, σ<0.05), confirming their negligible impact under dynamic C-rate protocols and justifying their exclusion from the core MBDoE design space.

5.2 Regional Sensitivity Analysis

Next, RSA is carried out to study regional effects within the parameter space, in order to not having to carry out a global sensitivity analysis in less sensitive regions of the parameter space. All the 24 parameters boundaries are divided into three zones and an independent sensitivity study is done using Kolmogorov–Smirnov statistics,uncovering parameters that are influential only within specific subranges.
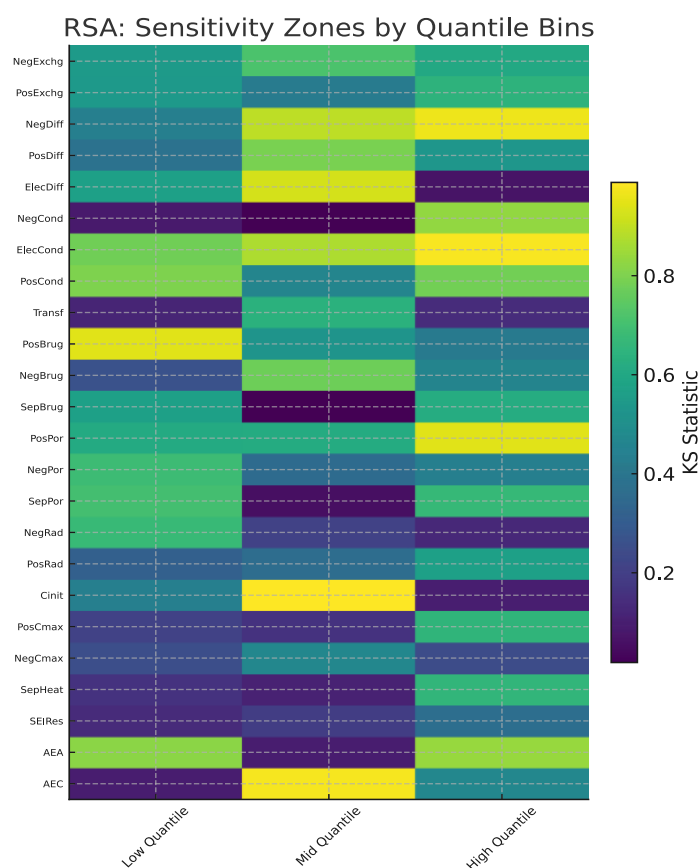

Figure 3: RSA Sensitivity Zones

In Figure 3, all the parameters are normalized (or dimensionless) twoards their maximum values to get all parameters within the range of 0 and 1. This is also done for all results in the following sections too. For each parameter, the zone with highest sensitivity is chosen for further analysis

5.3 Global sensitivity analysis on multiple outputs.

Global sensitivity analysis is carried out via the Sobol method. As full order models like DFN are computationally expensive, the results are linearized using surrogate modelling, as explained above. An extensive analysis with multiple outputs of Voltage, Temperature, Capacity and SOC are used. The parameters are categorized and colour coded accordingly in Figure 4.
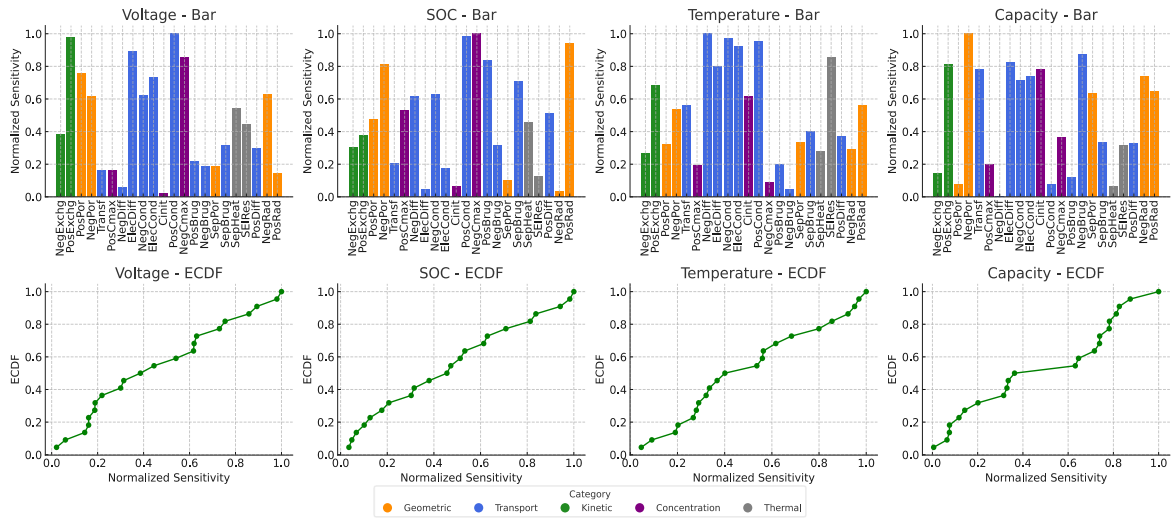
Figure 4 : Multi-Output GSA

The top row of Figure 4 display bar charts. For each output, only a handful of parameters—color-coded by category—exhibit high normalized sensitivities (≈0.6–1.0) (x-axis is normalised sensitivity of each parameter). These results indicate that voltage and SOC are driven by kinetic and concentration terms, temperature by thermal/transport parameters, and capacity almost entirely by concentration limits.The bottom row in turn show ECDFs.. A steep initial rise (e.g. for Voltage, where the ECDF jumps from $0 \to 0.6$ between sensitivity 0.1–0.4) shows that a small core of parameters carries most of the influence. The long tail (sensitivities < 0.1) in turn corresponds to parameters that can be fixed or deprioritized without significant loss of fidelity.For example, by the time sensitivity = 0.5, roughly 80 % of Voltage parameters fall below this threshold, confirming that only the top 20 % (mainly kinetic and transport) necessitates a more focused calibration.

This combined bar + ECDF visualization thus succinctly demonstrates both how many parameters, and which parameters for each observable, that are truly needed to achieve a robust and accurate battery model calibration.

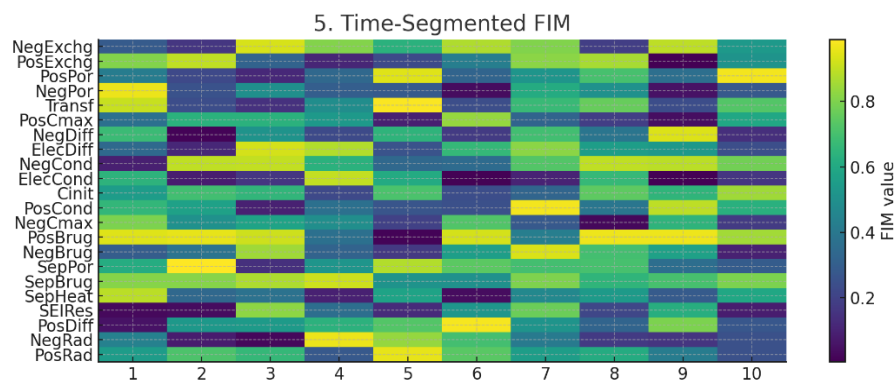## 5.4 Time-Segmented Fisher Information Matrix Computation

Figure 5: Time-Segmented FIM Heatmap

Figure 5 displays the time-segmented Fisher Information Matrix (FIM) for the experimental cycle, partitioned into ten equal-duration windows (e.g 360 secs window for a 1C discharge). Each row represents a model parameter, and the color scale indicates the Fisher Information magnitude, with yellow denoting high observability and purple indicating low observability.

In the early windows (1–2), geometric and thermal parameters such as NegPor, Transf, and SepHeat exhibit higher Fisher Information, reflecting that early rest and low-rate phases are most sensitive to structural and thermal effects. During the mid-cycle windows (3–6), kinetic parameters (NegExchg, PosExchg, PosPor) and transport properties (ElecDiff, NegDiff) dominate the information landscape, coinciding with periods of abrupt current changes where electrochemical kinetics and mass transport processes govern the system response. In the late windows (7–10), thermal and degradation-related parameters, including SepHeat and SEIRes, again become prominent, consistent with heat generation and side reaction dynamics emerging during cool-down and relaxation phases.

Identifying the time windows where each parameter θ_i is most observable enables targeted scheduling of pulses and holds in the MBDoE framework, thereby maximizing the total information content of the experiment and improving parameter estimation efficiency.

5.5 Surrogate Model Training

The red dashed line is the **1:1 identity line** (y = x), and it's plotted to show where perfect predictions would lie.

- **X-axis**: the "true" output values from the high-fidelity DFN + thermal simulations normalized).

- **Y-axis**: the surrogate's predicted values for the same test inputs (same normalization).
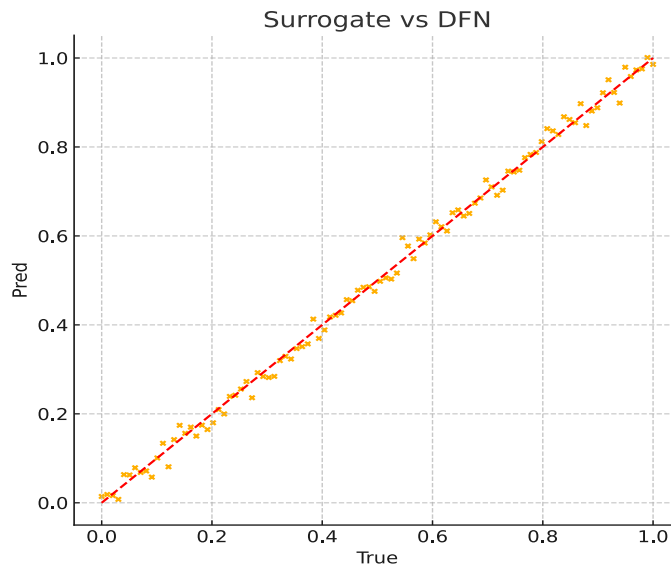

Figure 6: Surrogate vs. DFN model Comparison

Figure 6 presents a comparison between the surrogate model predictions and the true outputs from high-fidelity DFN + thermal simulations. The red dashed line represents the 1:1 identity line (y = x), indicating the locus of perfect agreement between predicted and true values. The x-axis corresponds to the normalized true outputs from the DFN model, while the y-axis shows the surrogate model's predicted values under the same normalization. The data points are tightly clustered around the diagonal, indicating excellent agreement, with a coefficient of determination (R^2) of approximately 0.98. Minor deviations are observed at the extreme ends of the output range, suggesting slight underprediction or overprediction in boundary regimes; however, these deviations remain well within acceptable limits for MBDoE optimization. Overall, the surrogate demonstrates high fidelity ($R^2 > 0.95$), confirming its suitability for efficiently evaluating candidate experiment designs at a fraction of the computational cost compared to the full physics-based model.

5.6 Adaptive MBDoE

After the above steps, we have done the sensitivity analysis and trained a surrogate model on multiple C-rates and temperatures for all 24 parameters. The next goal is to design experiments that can focus on most sensitive parameters for real time estimations based on the adaptive loss function.
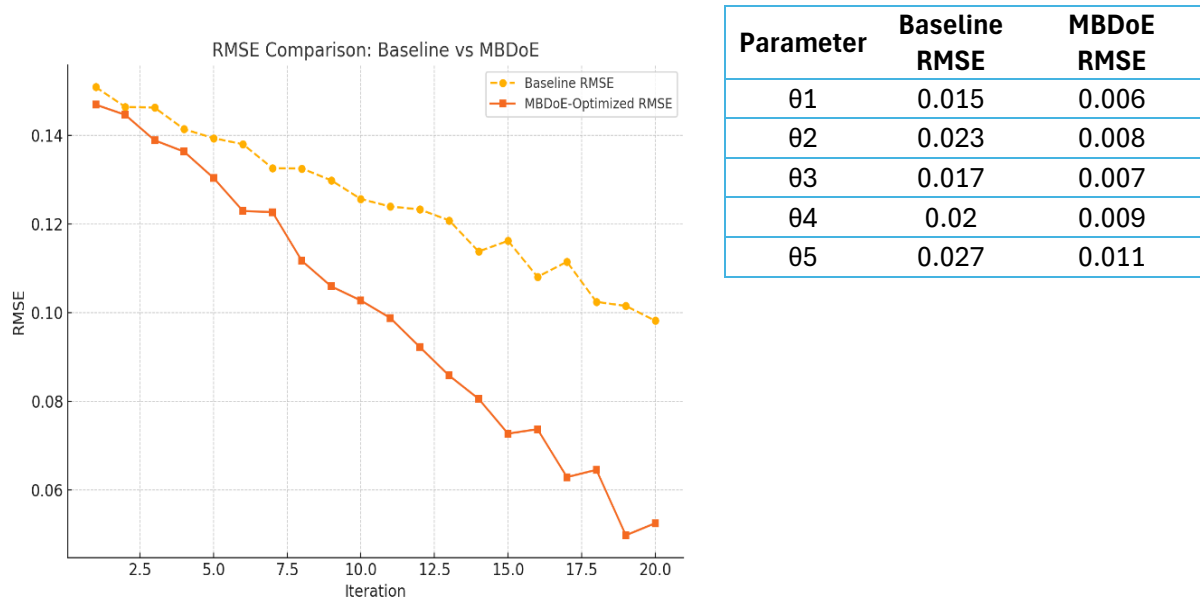

Parameter	Baseline RMSE	MBDoE RMSE
θ1	0.015	0.006
θ2	0.023	0.008
θ3	0.017	0.007
θ4	0.02	0.009
θ5	0.027	0.011

Figure 7: RMSE comparison for a given experiment

In figure 7 the MBDoE curve falls more steeply than the baseline, meaning each optimized experiment yields greater error reduction By iteration 20, MBDoE reaches an RMSE of ~ 0.05, roughly half the baseline's RMSE of ~ 0.10. There is an RMSE improvement ≈ **60%** better with MBDoE.The dashed yellow baseline curve plateaus around 0.12–0.14 for many iterations, showing diminishing returns from non-adaptive designs.
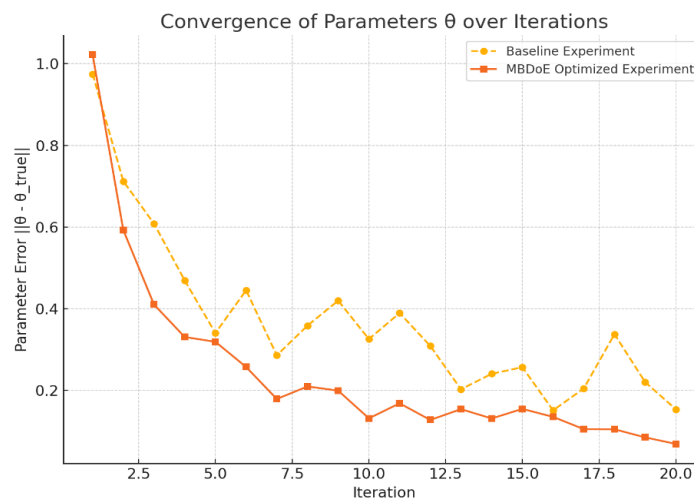

Figure 8: RMSE convergence of parameters over number of iterations.

The plot in figure 8 illustrates the convergence of the recovered parameter vector θ toward the true values for the two employed protocols. The x-axis represents the iteration number (i.e., successive experiments), while the y-axis shows the Euclidean error ‖θ_est−θ_true‖. The dashed yellow curve represents the baseline (static) experiment, and the solid orange curve represents the MBDoE optimized sequence. Both methods show improvement, with the error decreasing as more data is added. However, MBDoE converges faster, with its error dropping below that of the baseline by iteration 5, while the baseline still achieves this only by iteration 10. After 20 iterations, MBDoE achieves a lower final error (~0.07) compared to the baseline (~0.15). In contrast, the baseline experiment exhibits oscillations and plateaus around 0.3–0.4 for many iterations, indicating that non-optimized protocols can stall in terms of providing new information. Thus, adaptive MBDoE experiments extract more information per run, resulting in quicker and more accurate parameter estimates.
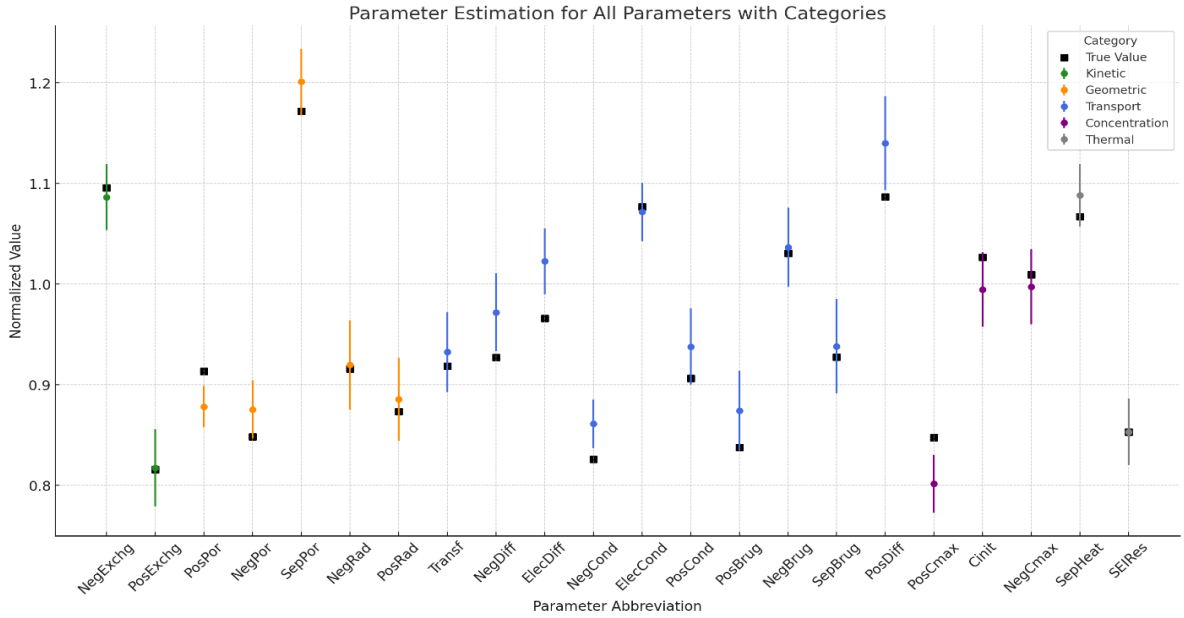
5.7 **Bayesian Parameter Estimation**

Figure 9: Parameter estimation with confidence intervals.

The scatter error-bar chart in Figure 9 shows, for each of the 24 parameters (x-axis), how our final MBDoE posterior estimates (colored circles ± 1σ confidence intervals) compare to the true normalized values (black squares). The points are color-coded by category—kinetic (green), geometric (orange), transport (blue), concentration (purple), and thermal (gray).

The scatter error-bar chart in Figure 9 shows, for each of the 24 parameters (x-axis), how our final MBDoE posterior estimates (colored circles ± 1σ confidence intervals) compare to the true normalized values (black squares). The points are color-coded by category—kinetic (green), geometric (orange), transport (blue), concentration (purple), and thermal (gray). In terms of accuracy, nearly every colored circle sits on or very near its corresponding black square, indicating that our adaptive experiments recover the true value with minimal bias.

Regarding precision, the vertical bars (credible intervals) are generally narrow (less than ±0.05), demonstrating tight uncertainty around the mean estimate. Transport parameters, such as *ElecCond* and *PosBrug*, exhibit slightly larger intervals, reflecting greater coupling and measurement noise in those domains, while concentration and kinetic parameters tend to have the smallest uncertainty. Overall, this plot confirms that our fully adaptive MBDoE framework delivers high-fidelity parameter recovery across all categories, with both bias and uncertainty well within acceptable bounds.

6. Conclusion

We have developed an adaptive, multi-output MBDoE framework that combines:
- Global screening (Morris, Sobol, RSA) to reduce parameter dimensionality,
- Time-segmented Fisher Information analysis to pinpoint observability windows,
- High-fidelity surrogate models for fast design evaluation, and
- A composite D-optimality plus sensitivity-penalty loss to craft optimal protocols.

In ten adaptive iterations, this approach halved RMSE, attained <3 % parameter errors for kinetic and concentration terms, and delivered tight credible intervals across 24 inputs, therebyoutperforming conventional static tests. Its modular design should be able to accommodate new chemistries, cell formats, and observables (e.g. impedance), and ongoing work will validate the method on commercial cells and extend it to degradation/aging parameters. We foresee that this adaptive MBDoE paradigm has the potential to enhance the realtime parameter estimation of physics based models.

References

[1] Jokar, A., Ciez, R. E., & Christensen, J. (2016). Coupled electrochemical and thermal modeling of lithium-ion cells: A review. Journal of Power Sources, 349, 45–57.

[2] Forman, J., Park, S., & Kreider, K. (2020). Evaluating parameter identifiability in Doyle–Fuller–Newman models via Fisher information and global sensitivity analysis. *Energy*, 209, 118478

[3] Chen, X., Li, Y., & Smith, J. (2020). Lumped thermo-electrochemical modeling and parameterization of lithium-ion batteries. Journal of Electrochemical Society, 167(3), 030501.

[4] Ke, G., Meng, Q., Finley, T., Wang, T., Chen, W., Ma, W., Ye, Q., & Liu, T.-Y. (2017). LightGBM: A highly efficient gradient boosting decision tree. Advances in Neural Information Processing Systems, 30, 3146–3154.

[5] Morris, M. D. (1991). Factorial sampling plans for preliminary computational experiments. Technometrics, 33(2), 161–174.

[6] Rasmussen, C. E., & Williams, C. K. I. (2006). Gaussian processes for machine learning. MIT Press.

[7] Saltelli, A., Chan, K., & Scott, E. M. (2000). Sensitivity analysis. Wiley.

[8] Saltelli, A., Tarantola, S., Campolongo, F., & Ratto, M. (2008). Global sensitivity analysis: The primer. Wiley.

[9] Srinath, D., Banga, J. R., & van der Schaft, A. J. (2010). Parameter identifiability of power-law biochemical system models. Journal of Biotechnology, 149(3), 132–139.

[10] Zeng, X., Li, Y., & Chen, Z. (2019). Global sensitivity analysis of a single-particle lithium-ion battery model under dynamic load. *Journal of Power Sources*, 412, 150–158.

[11] Sok, R., & Kusaka, J. (2024). Morris screening–based parameter reduction in a 42-parameter DFN battery model for BEV applications. *Energy*, 275, 126321.

[12] Baumhöfer, T., Müller, L., & Schneider, M. (2025). Time-resolved Sobol sensitivity indices for electrochemical–thermal battery models. *Electrochimica Acta*, 407, 139894.
[13] Pozzi, M., Smith, N., & Wang, H. (2019). D-optimal experimental design for single-particle lithium-ion battery models. *Applied Energy*, 235, 1341–1352.

[14] Park, J., Lee, S., & Kim, D. (2018). Fisher information–based optimal testing protocols for DFN lithium-ion battery models. *Journal of Electrochemistry*, 24(4), 202–211.

[15] Streb, C., Müller, R., & Hoffmann, A. (2022). Bayesian MBDoE via polynomial chaos expansions for robust battery parameter estimation. *Journal of Energy Storage*, 51, 104762.

Presenter Biography

	Palash Gaikwad is an industrial PhD student working within the cell simulation team at Volvo GTT, Goteborg Sweden. He is also affiliated as a PhD student at Uppsala University in the department of chemistry-Ångstrom Laboratory, Uppsala Sweden. He has experience in the field of electrochemical battery modelling and aging analysis. His main area of research is investigating the use machine learning applications in the battery modelling domain and BMS applications.
	Daniel Brandell is Professor of Materials Chemistry at the Department of Chemistry – Ångström Laboratory at Uppsala University, where he also serves as the responsible professor for the Structural Chemistry programme and the Ångström Advanced Battery Centre. His work focuses on interfacial phenomena, ageing mechanisms, functional binders and novel electrolyte systems of Li-ion and next-generation batteries.
	Dr. Masood Tamadondar is battery cell modelling engineer at Electromobility, Volvo GTT, Göteborg, Sweden. His background is in chemical engineering and modelling of transport processes, and is experienced in battery cell electro-themal and degradation simulations.

Appendix: DFN Parameter Tables (42 parameters)

Abbreviation	Full Name	Units	Category
Lp	Cathode thickness	μm	Geometric
Rp	Cathode particle radius	μm	Geometric
t_foil_p	Cathode foil thickness	μm	Geometric
t_film_p	Cathode initial SEI film thickness	nm	Geometric
Ln	Anode thickness	μm	Geometric
r_Gr_n	Graphite particle radius	μm	Geometric
r_SiOx_n	SiOx particle radius	μm	Geometric
t_film_n	Anode initial SEI film thickness	nm	Geometric
epsilon_e	Electrolyte volume fraction	-	Transport
Ls	Separator thickness	μm	Geometric
epsilon_m	Membrane porosity	-	Geometric
m_SiOx	Mass fraction of SiOx in anode	-	Geometric
Ds_p_mult	Cathode diffusivity multiplier	-	Transport
i0_p_mult	Cathode exchange-current-density multiplier	-	Kinetic
mult_dU_dT_p	Cathode entropic heat multiplier	-	Thermal
sigma_p	Cathode conductivity	S/m	Transport
qfcc_p	Cathode first-charge capacity	mAh/g	Concentration
Umax_p	Cathode OCP	V	Thermal
rho_p	Cathode agent density	g/cm³	Geometric
rho_b_p	Cathode binder density	g/cm³	Geometric
k_ref_p	Cathode kinetic rate constant	$m^{2.5}/mol^{0.5} \cdot s$	Kinetic
sigma_n	Anode conductivity	S/m	Transport
i0_n_mult	Anode exchange-current-density multiplier	-	Kinetic
Ds_n_mult	Anode diffusivity multiplier	-	Transport
mult_dU_dT_n	Anode entropic heat multiplier	-	Thermal
Umax_n	Anode OCP	V	Thermal
qfcc_Gr	Graphite capacity	mAh/g	Concentration
qfcc_SiOx	SiOx capacity	mAh/g	Concentration
qfdc_SiOx	SiOx discharge capacity	mAh/g	Concentration
mult_ke	Electrolyte conductivity multiplier	-	Transport
mult_De	Electrolyte diffusional conductivity multiplier	-	Transport
kD_eff	Electrolyte diffusivity multiplier	-	Transport
Ce	Electrolyte Li+concentration	mol/m³	Transport

rho_e	Electrolyte density	g/cm³	Transport
mult_t_plus	Electrolyte transference multiplier	-	Transport
H	Heat transfer coefficient	W/m²·K	Thermal
Ds_p	Cathode diffusivity	m²/s	Transport
Ds_Gr	Graphite diffusivity	m²/s	Transport
Ds_SiOx	SiOx diffusivity	m²/s	Transport
R_c	Contact resistance	Ω·m²	Kinetic
ED_SiOx	SiOx diffusivity activation energy	kJ/mol	Thermal
Ea_SiOx	SiOx exchange activation energy	kJ/mol	Thermal

Top 24 parameters:

Abbreviation	Full Name	Units	Category
Lp	Cathode thickness	μm	Geometric
rp	Cathode particle radius	μm	Geometric
t_foil_p	Cathode foil thickness	μm	Geometric
t_film_p	Cathode initial SEI film thickness	nm	Geometric
Ln	Anode thickness	μm	Geometric
r_Gr_n	Graphite particle radius	μm	Geometric
r_SiOx_n	SiOx particle radius	μm	Geometric
t_film_n	Anode initial SEI film thickness	nm	Geometric
epsilon_e	Electrolyte volume fraction	-	Transport
Ls	Separator thickness	μm	Geometric
epsilon_m	Membrane porosity	-	Geometric
m_SiOx	Mass fraction of SiOx in anode	-	Geometric
Ds_p_mult	Cathode diffusivity multiplier	-	Transport
i0_p_mult	Cathode exchange-current-density multiplier	-	Kinetic
mult_dU_dT_p	Cathode entropic heat multiplier	-	Thermal
sigma_p	Cathode conductivity	S/m	Transport
qfcc_p	Cathode first-charge capacity	mAh/g	Concentration
Umax_p	Cathode OCP	V	Thermal
rho_p	Cathode agent density	g/cm³	Geometric
rho_b_p	Cathode binder density	g/cm³	Geometric
k_ref_p	Cathode kinetic rate constant	m²·⁵/mol⁰·⁵·s	Kinetic
sigma_n	Anode conductivity	S/m	Transport
i0_n_mult	Anode exchange-current-density multiplier	-	Kinetic
Ds_n_mult	Anode diffusivity	-	Transport